

BijjectiveRemesh: Maintaining Bijjective Mappings for Data Transfer Across Remeshed Manifolds

LEYI ZHU, New York University, USA

MICHAEL TAO, New York University, USA

YIXIN HU, Tencent America, USA

DANIELE PANOZZO, New York University, USA

DENIS ZORIN, New York University, USA

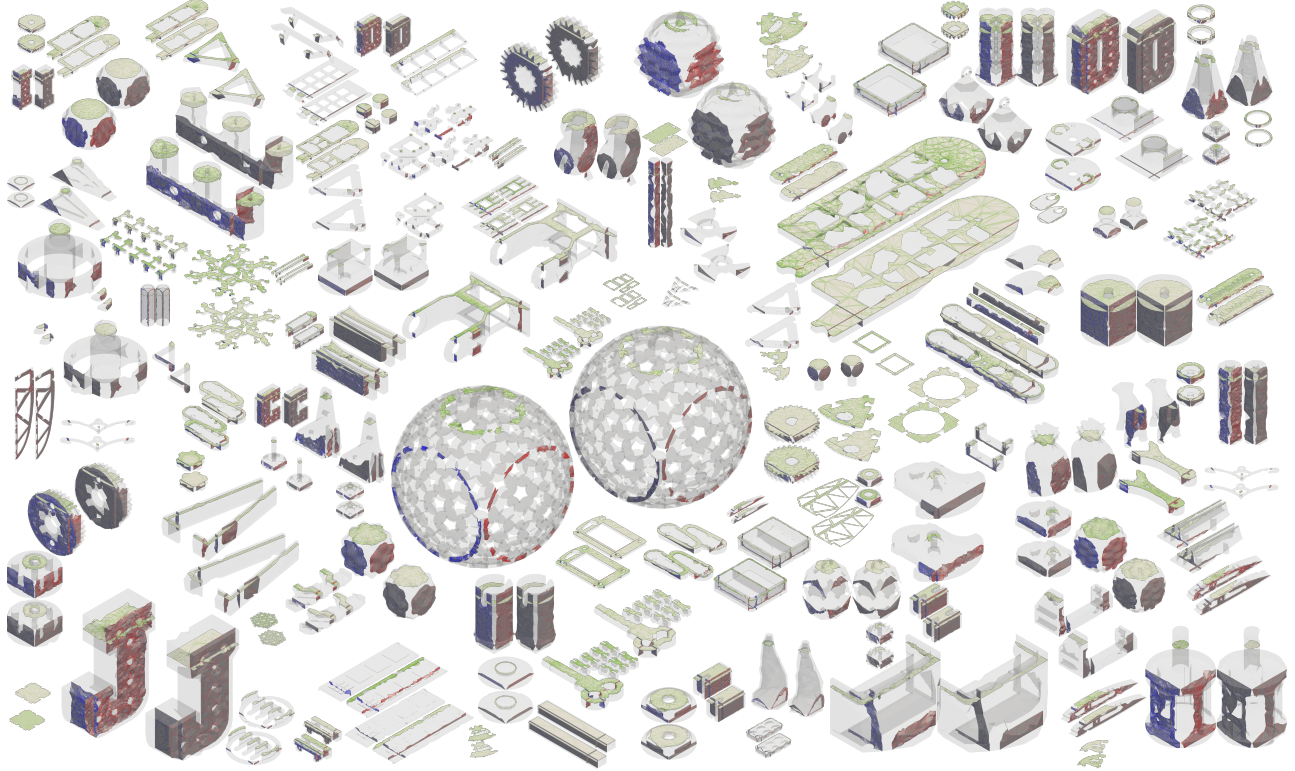


Fig. 1. **Bijjective surface tracking through tetrahedral mesh simplification.** We track axis-aligned planar surfaces (parallel to the xy , xz , and yz planes) through tetrahedral mesh simplification on models from the Thingi10K dataset [Zhou and Jacobson 2016]. For each model, surfaces are sampled on the simplified output mesh $\mathcal{M}_{\text{output}}$ (right) and back-tracked to the original mesh $\mathcal{M}_{\text{input}}$ (left). Our bijective framework rigorously preserves the intersection topology among surfaces: where surfaces intersect on the output, they intersect consistently on the input, maintaining the combinatorial structure of intersection curves throughout the tracking process.

We introduce *BijjectiveRemesh*, a robust algorithm for maintaining a continuous, bijective mapping across complex remeshing sequences on both 2D triangle surfaces and 3D tetrahedral meshes. Unlike traditional data transfer methods that rely on interpolation or projection, our approach constructs a mathematically rigorous composite map $f : \mathcal{M}_{\text{input}} \rightarrow \mathcal{M}_{\text{output}}$ by chaining local bijective atlases defined for each primitive operation.

Our framework represents the overall mapping as a composition of local bijective atlases, one per remeshing operation. Building upon successive self-parameterization (SSP) [Liu et al. 2021], we introduce a *Shared Scaffold* structure for 2D triangle meshes that enforces global bijectivity through

local orientation preservation. We extend this approach to handle edge splits, edge swaps, and vertex smoothing beyond the original edge collapses. For 3D tetrahedral meshes, we generalize the local atlas construction using Steinitz’s Theorem and Maxwell-Cremona lifting to ensure valid embeddings. This enables exact tracking of geometric entities—points, curves, and surfaces—across remeshing, with applications from texture transfer to volumetric simulations.

1 Introduction

Remeshing is ubiquitous in computer graphics and scientific computing, encompassing tasks such as quality improvement, resolution adaptation, and artifact repair. A fundamental challenge across all these operations is *data transfer*: propagating scalar fields, texture

Authors’ Contact Information: Leyi Zhu, New York University, USA; Michael Tao, New York University, USA; Yixin Hu, Tencent America, USA; Daniele Panozzo, New York University, USA; Denis Zorin, New York University, USA.

coordinates, material attributes, or boundary conditions from the original mesh to the remeshed version with high fidelity. As meshes undergo decimation, refinement, or optimization, maintaining precise correspondences between initial and remeshed states is critical to prevent information loss and numerical diffusion.

Conventional solutions for maintaining correspondences between meshes [Kobbelt et al. 1998] rely on heuristics such as barycentric interpolation or closest-point projections [Botsch et al. 2010]. While effective for minor adjustments, these methods lack topological guarantees. Furthermore, when topological operations induce substantial changes (e.g., edge collapses or swaps), these heuristic correspondence often fail to be bijective, causing artifacts like UV seam tearing, texture deviation, or loss of feature lines. Constructing a global bijective parameterization could resolve these issues, but is computationally prohibitive and prone to failure on complex non-disk-topology shapes [Kraevoy and Sheffer 2004].

We propose a scalable framework that maintains strict bijective mappings throughout remeshing, enabling accurate data transfer between the original and remeshed states. Rather than computing a single global parameterization, our method encodes the overall map as a composition of local maps induced by atomic operation. This mesh evolution "history", enables precise bidirectional data transfer regardless of connectivity changes.

Our approach builds on two key ideas. First, for 2D triangle meshes, we construct local atlases using a shared scaffold structure [Jiang et al. 2017] that ensures bijectivity through locally injective optimization [Rabinovich et al. 2017]. Second, for 3D tetrahedral meshes, we leverage Steinitz’s Theorem [Ribó Mor et al. 2011] to construct convex polyhedral embeddings that geometrically prevent tetrahedral overlaps. These bijective local atlases enable robust tracking of geometric entities—including points, curves, and surfaces—throughout complex remeshing sequences. We demonstrate our framework on applications including texture transfer across remeshed models Figures 9 and 10 and preserving organ segmentations in medical CT data under mesh adaptation (Figure 13) and validate our topology preservation on the Thingi10K dataset [Zhou and Jacobson 2016].

2 Related Work

Maintaining bijective correspondences is a long-standing challenge in geometry processing, spanning surface parameterization, volumetric mapping, and attribute transfer.

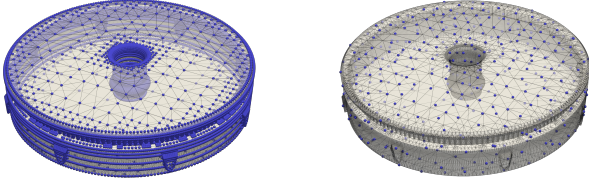
Strict Surface Homeomorphisms. Bijective surface parameterization traditionally relied on Tutte’s embedding theorem [Tutte 1963], which guarantees an injective mapping for 3-connected planar graphs into convex domains using barycentric coordinates [Floater 2003]. While robust, these linear methods are restricted to fixed convex boundaries. To allow boundary movement and minimize isometric distortion, non-linear optimization frameworks such as SLIM [Rabinovich et al. 2017] and Total Lifted Content (TLC) [Du et al. 2020] have been proposed. However, these methods either require an already-injective initialization or lack global bijectivity guarantees on complex topologies. Our 2D Shared Scaffold structure builds upon the Simplicial Complex Augmentation Framework

(SCAF) [Jiang et al. 2017], which ensures global bijectivity by reducing the problem to local orientation preservation within an augmented tessellation of the ambient space [Lipman 2014].

Volumetric Mapping and Topological Obstructions. Extending bijectivity guarantees to 3D tetrahedral meshes is significantly more complex due to topological obstructions. Notably, the 3D analog of Tutte’s theorem does not hold universally; even with convex boundaries, because internal tetrahedra can invert if the mesh contains specific forbidden minors like K_6 or $K_{3,3,1}$ [Alexa 2023; Floater and Pham-Trong 2006]. Constructive methods such as Simplicial Foliations [Campen et al. 2016] and the Shrink-and-Expand (SaE) framework [Nigolian et al. 2023, 2024] provide theoretical guarantees for shellable meshes but often incur extreme computational costs and memory-intensive mesh refinement. In contrast, our approach utilizes Steinitz’s Theorem [Steinitz 1922] and Maxwell-Cremona lifting [Ribó Mor et al. 2011] to construct local convex polyhedral embeddings for boundary operations. This ensures validity by exploiting the geometric property that convexity of the boundary polyhedron prevents interior overlap, avoiding the need for expensive global constructive schemes.

Mapping Preservation and Attribute Transfer. The "Bijective Prism Shell" [Jiang et al. 2020, 2021] establishes a common domain for spatially close surfaces by constructing a volumetric shell between them, though the approach is limited to surfaces within a narrow distance threshold and requires careful shell thickness tuning. Another direction is the use of "common triangulations" [Schmidt et al. 2023], which decouple map resolution from input complexity by adaptively refining a shared triangulation. However, this approach is restricted to genus-0 surfaces (mapping via the sphere) and loses the remeshing tracking sequence, requiring manual selection of landmark point pairs. Alternative approximate methods such as reversible harmonic maps [Ezuz et al. 2019] and low-resolution correspondence [Maggioli et al. 2024] trade accuracy for efficiency, but inherently incur information loss during transfer due to their continuous relaxation or downsampling strategies.

The closest work to ours is the successive self-parameterization (SSP) framework [Liu et al. 2021], which constructs bijective mappings by composing local atlases across remeshing operations. The atlases are constructed by a joint-flattening strategy where the 3D coordinates of pre- and post-operation patches (the localized mesh regions affected by each operation) are simultaneously parameterized into a shared 2D domain. While this approach successfully distributes distortion between mesh states, it suffers from two key limitations: First, the optimization lacks robustness guarantees and can fail to converge or produce inverted elements when mesh quality is poor. We observe frequent failures on models from the Thingi10K dataset [Zhou and Jacobson 2016]—for instance, model #1706476 exhibits failure of SSP because it prevents any collapse operations from completing (Figure 2). Second, SSP is designed specifically for edge collapse operations in the context of mesh coarsening and does not generalize to other remeshing primitives that we support, such as edge splits (for refinement), edge swaps (for quality improvement), or vertex smoothing (for geometry optimization). Additionally, the framework does not extend to 3D tetrahedral meshes, where boundary operations require fundamentally different geometric constructions.



(a) SSP method fails to complete any edge collapses (b) Our method robustly generates coarse-to-fine mapping

Fig. 2. Comparison on Thingi10K model #1706476. We visualize the coarse-to-fine mapping by transferring points from the decimated mesh back to the original fine mesh using successive parameterization. **Left:** The SSP framework [Liu et al. 2021] fails during optimization, preventing any edge collapse operations from completing. **Right:** Our shared scaffold method successfully constructs bijective mappings throughout the decimation process, enabling robust data transfer between mesh representations.

3 Method

Given an input manifold mesh $\mathcal{M}_{\text{input}}$ and a sequence of remeshing operations $\mathcal{O} = \{o_1, o_2, \dots, o_n\}$, our goal is to maintain a continuous, bijective mapping $f : \mathcal{M}_{\text{input}} \rightarrow \mathcal{M}_{\text{output}}$ throughout the entire remeshing process. We assume the input \mathcal{M} is a manifold simplicial complex, which can be either a 2D triangle mesh embedded in \mathbb{R}^3 or a 3D tetrahedral mesh in \mathbb{R}^3 . The operation sequence \mathcal{O} may consist of various topological and geometric modifications, including edge collapses, edge splits, edge swaps, and vertex smoothing.

We follow the insight of Liu et al. [2021] by noting that, while the cumulative effect of remeshing is global, each individual operation $o_i : \mathcal{M}_{i-1} \rightarrow \mathcal{M}_i$ only acts on a small, localized patch (the Region of Interest, Figure 3). We denote these local patches as $\mathcal{P}_i^{\text{before}} \subset \mathcal{M}_{i-1}$ and $\mathcal{P}_i^{\text{after}} \subset \mathcal{M}_i$, corresponding to the mesh state before and after the operation.

To construct a bijection between these two patches, we embed both into a shared geometric domain \mathcal{C}_i via embeddings $e_i^{\text{before}} : \mathcal{P}_i^{\text{before}} \rightarrow \mathcal{C}_i$ and $e_i^{\text{after}} : \mathcal{P}_i^{\text{after}} \rightarrow \mathcal{C}_i$. (Figure 7) This establishes a canonical bijection:

$$\varphi_i = (e_i^{\text{after}})^{-1} \circ e_i^{\text{before}} : \mathcal{P}_i^{\text{before}} \rightarrow \mathcal{P}_i^{\text{after}}. \quad (1)$$

Since the operation only modifies the local region, this local bijection extends to a global map $\varphi_i : \mathcal{M}_{i-1} \rightarrow \mathcal{M}_i$ that is the identity outside of $\mathcal{P}_i^{\text{before}}$. The global bijective mapping is then obtained by composition:

$$\Phi = \varphi_n \circ \varphi_{n-1} \circ \dots \circ \varphi_1. \quad (2)$$

This formulation allows us to handle diverse operations—including splits for refinement and collapses for coarsening—within a unified framework.

3.1 Constructing Bijective Maps Using Local Atlases

We use different bijective maps for triangle meshes and tetrahedral mesh, but they follow the same fundamental principle of constructing a shared parametric space through which we can perform mapping. The main difficulty is that remeshing can change the domain of the mesh, so our bijective maps must be able to handle a certain amount of distortion. For triangle meshes we are minimizing the distortion of points in 3D and most operations introduce some distortion to the geometry that must be minimized. On the other hand, tetrahedral meshes are embedded in 3D so for operations on the interior the identity map to \mathbb{R}^3 is the perfect bijective map and the entire challenge is how to deal with operations on the boundary that distort the domain of the tetrahedral mesh.

3.1.1 2D: Triangle Mesh. Background: Joint Flattening.

Our 2D approach builds upon the joint flattening strategy introduced by [Liu et al. 2021]. The key idea is to leverage the fact that when the patch $\mathcal{P}^{\text{before}}$ of a local operation lies on the interior of \mathcal{M}_{i-1} then $\mathcal{P}^{\text{after}}$ lies on the interior of \mathcal{M}_i and their boundaries remain geometrically consistent: $\partial\mathcal{P}^{\text{before}} \equiv \partial\mathcal{P}^{\text{after}}$. This allows both patches to be parameterized into a shared 2D domain by minimizing a joint distortion energy:

$$\min_{\mathbf{U}} E(\mathcal{P}^{\text{before}}, \mathbf{U}^{\text{before}}) + E(\mathcal{P}^{\text{after}}, \mathbf{U}^{\text{after}}) \quad (3)$$

subject to shared boundary coordinates:

$$\mathbf{u}_v^{\text{before}} = \mathbf{u}_v^{\text{after}}, \quad \forall v \in \partial\mathcal{P}. \quad (4)$$

where $\mathbf{U}^{\text{before}}$ and $\mathbf{U}^{\text{after}}$ are the UV coordinates for all vertices in $\mathcal{P}^{\text{before}}$ and $\mathcal{P}^{\text{after}}$ respectively, $\mathbf{u}_v \in \mathbb{R}^2$ denotes the UV position of vertex v , and E is a standard distortion metric such as Symmetric Dirichlet [Smith and Schaefer 2015] or ARAP energy [Sorkine and Alexa 2007].

For edge collapses on the boundary, where vertex i is collapsed toward vertex j , a colinearity constraint is applied: the collapsed position \mathbf{u}_i must remain colinear with its neighboring boundary vertices j and k in the parametric domain. Although this treatment ensures the boundary shape remains well-defined for both connectivity states, it does not guarantee bijectivity: the optimization can produce overlapping or inverted triangles, particularly on poor-quality meshes. To rigorously enforce bijectivity, we augment this framework with a *shared scaffold structure*. We first review the Simplicial Complex Augmentation Framework (SCAF) [Jiang et al. 2017] that provides the theoretical foundation, then describe our construction of the shared scaffold for joint flattening.

Background: Simplicial Complex Augmentation Framework. SCAF guarantees bijectivity by adding an auxiliary "scaffold" triangulation around a mesh patch to make it so that global bijectivity can be preserved by maintaining local injectivity. Given a 2D mesh patch \mathcal{P} to be parameterized, SCAF constructs a scaffold \mathcal{S} between \mathcal{P} and its bounding box so $\mathcal{D} = \mathcal{S} \cup \mathcal{P}$ is a simplicial complex that tessellates a convex domain (Figure 4).

The critical property of SCAF is that any potential self-intersections of \mathcal{P} are captured by checking for *local injectivity* (i.e., has positive Jacobian determinant per element) on \mathcal{D} so local and global bijectivity become identical. then the entire mapping is *globally bijective*.

As such, global overlaps can be reduced to per-element orientation checks. We can therefore apply locally injective optimization methods like SLIM [Rabinovich et al. 2017] with an orientation-preserving line search to optimize distortion while guaranteeing global bijectivity.

Shared Scaffold for Joint Flattening. Since $\mathcal{P}^{\text{before}}$ and $\mathcal{P}^{\text{after}}$ are both parameterized into the same 2D domain and share a common boundary $\partial\mathcal{P}$, we can naturally construct a *single* shared scaffold \mathcal{S} for *both* patches. Specifically, we form two augmented complexes:

$$\mathcal{D}^{\text{before}} = \mathcal{P}^{\text{before}} \cup \mathcal{S}, \quad \mathcal{D}^{\text{after}} = \mathcal{P}^{\text{after}} \cup \mathcal{S}. \quad (5)$$

We then minimize the joint distortion energy over the vertex positions of both augmented complexes:

$$\min_{\mathbf{U}} E(\mathcal{D}^{\text{before}}, \mathbf{U}^{\text{before}}) + E(\mathcal{D}^{\text{after}}, \mathbf{U}^{\text{after}}), \quad (6)$$

subject to:

- **Shared boundary:** $\mathbf{u}_v^{\text{before}} = \mathbf{u}_v^{\text{after}}$ for all $v \in \partial\mathcal{P}$.
- **Shared scaffold:** $\mathbf{u}_v^{\text{before}} = \mathbf{u}_v^{\text{after}}$ for all $v \in \mathcal{S}$.

By using SCAF and SLIM the result of our optimization is guaranteed to produce a globally bijective embedding of $\mathcal{P}^{\text{before}}$ and $\mathcal{P}^{\text{after}}$. Furthermore, since both patches share the same non-overlapping scaffold \mathcal{S} , a bijective correspondence between $\mathcal{P}^{\text{before}}$ and $\mathcal{P}^{\text{after}}$ can be established through the resulting common parametric domain. Figure 4 illustrates this shared scaffold framework.

Application to Different Operation Types. The shared scaffold framework applies uniformly across various remeshing operations. Figure 3 illustrates the local patches for each operation type. Using the open star St ([Munkres 2018]), the local patches we use are:

- (1) *Edge Collapse* (i, j) $\rightarrow k$: $\mathcal{P}^{\text{before}} = \text{St}(i) \cup \text{St}(j)$ (union of 1-rings of both vertices), $\mathcal{P}^{\text{after}} = \text{St}(k)$ (1-ring of merged vertex).
- (2) *Edge Split* on edge (i, j) creating vertex k : $\mathcal{P}^{\text{before}} = \text{St}(i, j)$ (triangles incident to the edge), $\mathcal{P}^{\text{after}} = \text{St}(k)$ (1-ring of new vertex).
- (3) *Edge Swap*: $\mathcal{P}^{\text{before}}$ and $\mathcal{P}^{\text{after}}$ are both the two triangles sharing the edge.
- (4) *Vertex Smoothing* of vertex v : $\mathcal{P}^{\text{before}} = \mathcal{P}^{\text{after}} = \text{St}(v)$ (1-ring of the vertex, connectivity unchanged).

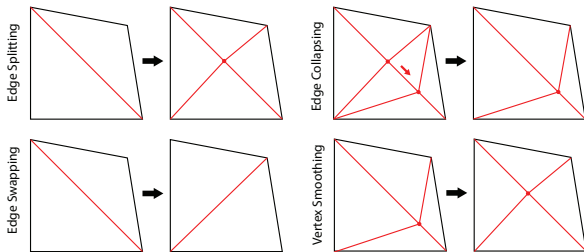
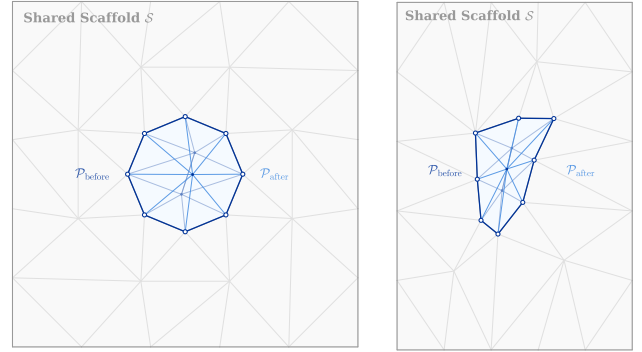


Fig. 3. Patches for different remeshing operations.



(a) Shared Scaffold Structure (b) After Joint Optimization

Fig. 4. Shared scaffold framework for bijective atlas construction. (a) Both $\mathcal{P}^{\text{before}}$ and $\mathcal{P}^{\text{after}}$ are embedded within the same scaffold \mathcal{S} (gray), sharing a common boundary $\partial\mathcal{P}$ (dark blue). (b) After joint optimization, the scaffold \mathcal{S} is deformed to minimize distortion while maintaining the sharing constraint ($\mathbf{u}_v^{\text{before}} = \mathbf{u}_v^{\text{after}}$ for all $v \in \mathcal{S} \cup \partial\mathcal{P}$). Local injectivity via SLIM optimization guarantees global bijectivity for both augmented complexes through the SCAF property, establishing bijective correspondence via the shared parametric domain.

3.1.2 3D: Tetrahedral Mesh. Recall that for tetrahedral meshes interior operations constructing bijective mapping is trivial and no deformation is necessary at all. In such cases, we extract the affected region (the closed star of the operation) as the local atlas and use identity mapping between the old and new connectivity to maintain bijectivity.

The primary challenge arises when handling **boundary operations**, which introduce geometric changes to the mesh surface. Of the four operations we choose use in our system, three can be implemented concisely:

Boundary Edge Split. Splitting a boundary edge does not alter the geometric shape of the boundary surface and only refine the mesh connectivity. Since the boundary geometry remains unchanged we can extract the affected local region and establish a canonical bijective correspondence, identical to the treatment of interior operations.

Boundary Vertex Smoothing. Vertex smoothing preserves the mesh connectivity while modifying vertex positions. In this case the set of tetrahedra in $\mathcal{P}^{\text{before}}$ and $\mathcal{P}^{\text{after}}$ have identical combinatorial structure and we presume that when a vertex of a tetrahedron is moved the points in the tetrahedron are all moved linearly. As such, we move each point in each tetrahedron so that its coordinate with respect to that tetrahedron’s barycentric coordinates remains the same before and after the operation.

Boundary Edge Swap. An edge swap decomposes into edge split followed by edge collapse. As the split introduces no distortion and we have to implement the collapse anyway we chose to implement the swap atlas as the composition of the split atlas and the collapse atlas.

3.1.3 Boundary Edge Collapse. The remaining atlas to describe is the **boundary edge collapse**, which genuinely alters the boundary

geometry and connectivity simultaneously. The object is, therefore, to construct a reparametrization that embeds both $\mathcal{P}^{\text{before}}$ and $\mathcal{P}^{\text{after}}$ into a consistent geometric domain, thereby establishing a bijective correspondence between them.

Consider a mesh \mathcal{M}_ℓ at step ℓ of the remeshing sequence, with boundary surface $\partial\mathcal{M}_\ell$. Suppose we perform a boundary edge collapse on edge (i, j) , yielding the updated mesh $\mathcal{M}_{\ell+1}$. Without loss of generality, we assume vertex i is collapsed toward vertex j .

Local Patch Extraction. Consider a boundary edge collapse operation that collapses vertex i toward vertex j . Let $\text{St}_\ell(v)$ denote the star of vertex v in \mathcal{M}_ℓ . We define the pre-collapse local patch as

$$\mathcal{P}^{\text{before}} = \text{St}_\ell(i). \quad (7)$$

The edge collapse removes every tetrahedron incident to edge (i, j) and replaces vertex i by j in the remaining tetrahedra. The post-collapse local patch $\mathcal{P}^{\text{after}} \subset \mathcal{M}_{\ell+1}$ consists of exactly those surviving tetrahedra, i.e., the tetrahedra in $\text{St}_\ell(i)$ that are not incident to edge (i, j) , with vertex i replaced by j .

Coplanarity Constraint. Similar to the 2D case for handling boundary edges, where we impose colinearity constraints to ensure a consistent boundary curve, in 3D we adopt an analogous strategy: during reparametrization, we constrain the boundary triangles affected by the collapse to lie in a common plane. Specifically, we require that the portions of the local patch boundary lying on the global mesh boundary,

$$\partial\mathcal{P}^{\text{before}} \cap \partial\mathcal{M}_\ell \quad \text{and} \quad \partial\mathcal{P}^{\text{after}} \cap \partial\mathcal{M}_{\ell+1}, \quad (8)$$

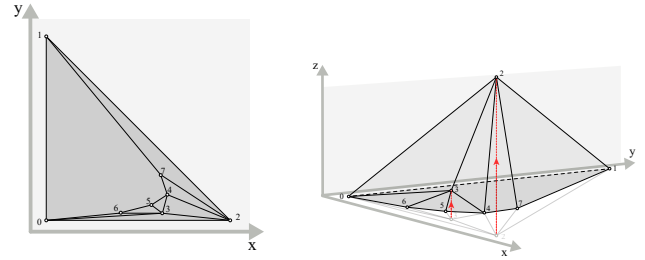
are reparametrized to lie in the same plane. Therefore, the collapse operation will not change the shape of the parametrization domain. Our problem then reduces to finding a reparametrization that satisfies this coplanarity constraint and can accommodate both the pre-collapse connectivity $\mathcal{P}^{\text{before}}$ and the post-collapse connectivity $\mathcal{P}^{\text{after}}$.

Reduction to Convex Polyhedron Construction. As established above, our problem reduces to finding a common reparametrization domain that can accommodate both $\mathcal{P}^{\text{before}}$ and $\mathcal{P}^{\text{after}}$. By Lemma A.1, this problem further simplifies to constructing a **convex polyhedron** that can simultaneously embed the boundaries $\partial\mathcal{P}^{\text{before}}$ and $\partial\mathcal{P}^{\text{after}}$. Crucially, to satisfy the coplanarity constraint, we require that the portions $\partial\mathcal{P}^{\text{before}} \cap \partial\mathcal{M}_\ell$ and $\partial\mathcal{P}^{\text{after}} \cap \partial\mathcal{M}_{\ell+1}$ are embedded onto a single face of this polyhedron. Specifically, the one-ring boundary vertices of vertex i , together with vertex i itself, must all lie on the same polyhedral face on the constructed convex polyhedron.

Combinatorial Formulation. We formulate this as a combinatorial problem. The boundary surface $\partial\mathcal{P}^{\text{before}}$ (equivalently, $\partial\mathcal{P}^{\text{after}}$) consists of two parts: (1) the k boundary triangles that do not contain vertex i , denoted f_0, \dots, f_{k-1} , and (2) the one-ring of vertex i on $\partial\mathcal{M}_\ell$, which forms an additional combinatorial face f_k (e.g., the face $[0, 6, 5, 4, 7, 1]$ in fig. 5a). Our question becomes: *Can the combinatorial graph G formed by $\{f_0, \dots, f_k\}$ be realized as the 1-skeleton of a convex polyhedron?*

The following classical result provides an affirmative answer:

THEOREM 3.1 (STEINITZ’S THEOREM). *A graph G is the 1-skeleton of a convex polyhedron if and only if G is simple, planar, and 3-connected.*



(a) Tutte barycentric embedding

(b) Maxwell-Cremona lifting

Fig. 5. Constructive algorithm for convex polyhedra embedding. (a) The Tutte embedding (Algorithm 1) produces a crossing-free 2D planar embedding with the outer triangle $f_0 = [0, 1, 2]$ fixed at positions $(0, 0)$, $(1, 0)$, and $(0, 1)$. Interior vertices (labeled 3–7) are positioned at their barycentric coordinates, yielding a valid planar layout. (b) The Maxwell-Cremona lifting (Algorithm 2) elevates this 2D embedding into a 3D convex polyhedron by assigning heights to each vertex.

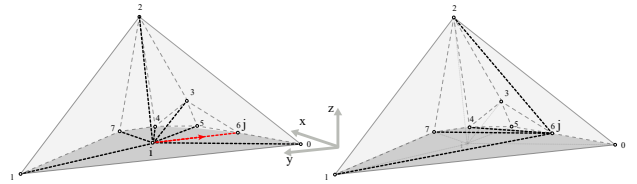


Fig. 6. Initial valid embedding for both $\mathcal{P}^{\text{before}}$ and $\mathcal{P}^{\text{after}}$. After constructing the convex polyhedron C via Algorithms 1 and 2, vertex i is placed at the barycenter of face f_k (the one-ring of i on the boundary). By Lemma A.1, this configuration is valid (non-overlapping) for both the pre-collapse connectivity (with edge (i, j)) and the post-collapse connectivity (where i has collapsed to j). This provides a valid starting point for joint optimization.

Constructive Algorithm. We follow the approach of [Ribó Mor et al. 2011] to realize a convex polyhedra embedding of the graph \mathcal{G} . We first select a triangle from $\{f_0, \dots, f_{k-1}\}$ as the outer boundary and compute a planar Tutte embedding [Tutte 1963] (fig. 5a). The Maxwell-Cremona lifting (fig. 5b) then elevates this 2D embedding into a 3D convex polyhedron by assigning heights to each vertex. Note that a naive approach—e.g., placing boundary vertices on one side and lifting interior vertices uniformly—does not in general produce a convex polyhedron, because the induced boundary edge stresses may violate the sign conditions required by the Maxwell-Cremona correspondence [Ribó Mor et al. 2011]. The full Tutte embedding with careful outer-face selection ensures these conditions are satisfied. The detailed pseudocodes are provided in Algorithms 1 and 2 in the Appendix.

Initial Embedding and Joint Optimization. A crucial requirement for our bijective optimization is that the initial embedding must be *flip-free* (all elements have positive orientation). Our optimization employs an orientation-preserving line search that can *maintain* this invariant but cannot *recover* from inverted elements—the AMIPS energy diverges to $+\infty$ for degenerate or inverted tetrahedra. The convex polyhedron construction provides this essential flip-free initialization: having constructed the embedding of \mathcal{G} , we recover

valid embeddings for both $\mathcal{P}^{\text{before}}$ and $\mathcal{P}^{\text{after}}$ by adding back their interior connectivity. By Lemma A.1, the convexity of the boundary polyhedron guarantees that these embeddings are non-overlapping and non-inverted. For $\mathcal{P}^{\text{before}}$, we additionally need to place vertex i inside face f_k . A simple choice is the barycenter of f_k :

$$\mathbf{p}_i = \frac{1}{|f_k|} \sum_{v \in f_k} \mathbf{p}_v,$$

where $|f_k|$ denotes the number of vertices in face f_k (see Fig. 6).

To obtain a low-distortion embedding, we perform joint optimization over both $\mathcal{P}^{\text{before}}$ and $\mathcal{P}^{\text{after}}$ simultaneously. We minimize the AMIPS [Fu et al. 2015] distortion energy:

$$\min_{\{\mathbf{p}_v\}} E_{\text{AMIPS}}(\mathcal{P}^{\text{before}}) + E_{\text{AMIPS}}(\mathcal{P}^{\text{after}}),$$

subject to the **coplanarity constraint**: vertex i remains on the plane containing face f_k . Specifically, let \mathbf{n}_k be the normal vector of face f_k , and let $v_0 \in f_k$ be any vertex on f_k . The constraint is:

$$(\mathbf{p}_i - \mathbf{p}_{v_0}) \cdot \mathbf{n}_k = 0.$$

The joint optimization framework, combined with the coplanarity constraint, yields a bijective mapping between $\mathcal{P}^{\text{before}}$ and $\mathcal{P}^{\text{after}}$ with minimal distortion, thus completing the construction of the local atlas for the boundary edge collapse operation. Note that the shared scaffold structure can naturally extend to this 3D setting as well.

3.2 Tracking Using Local Atlases

Having constructed local bijective atlases for each type of remeshing operation, we can now describe how to leverage these atlases to track geometric entities—points, curves, and surfaces—throughout the remeshing sequence. A key advantage of our bijective approach is that the local maps enable *bidirectional tracking*: we can map entities forward from the original mesh \mathcal{M} to the remeshed result \mathcal{M}' , or backward from \mathcal{M}' to \mathcal{M} . For clarity of exposition, we only consider the backward tracking perspective throughout this section, though the forward direction follows by symmetry.

3.2.1 Point Tracking. Point Representation. A point p on a simplicial mesh is represented by its barycentric coordinates with respect to a simplex:

$$p = (t, \mathbf{b}), \quad (9)$$

where t is the ID of a triangle in a triangle mesh or a tetrahedron in a tetrahedral mesh $\mathbf{b} = (b_0, b_1, \dots, b_d)$ are the barycentric coordinates with respect to the vertices of t ($d = 2$ for triangles, $d = 3$ for tetrahedra).

Backward Tracking Algorithm. Consider a remeshing operation $o_i : \mathcal{M}_{i-1} \rightarrow \mathcal{M}_i$ with its associated local atlas $(U_i, \mathcal{P}_i^{\text{before}}, \mathcal{P}_i^{\text{after}})$, where U_i is the shared parametric domain, $\mathcal{P}_i^{\text{before}} \subset \mathcal{M}_{i-1}$ and $\mathcal{P}_i^{\text{after}} \subset \mathcal{M}_i$ are the local patches affected by the operation, and U_i is the shared parametric domain into which both patches are embedded.

Now let us consider where to map a point $p' = (t', \mathbf{b}')$ on \mathcal{M}_i to \mathcal{M}_{i-1} given operation o_i . If it lies outside of $\mathcal{P}_i^{\text{after}}$ then it will not move, so its backtracked position is the trivially the same, i.e. $p = p'$.

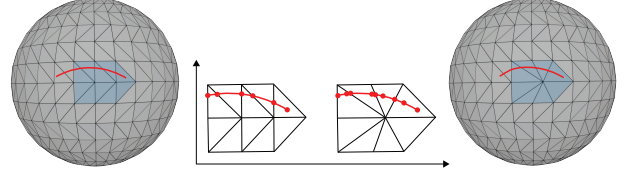


Fig. 7. Curve tracking via local atlas. The portion of the curve (red) on the patch is first mapped to the local atlas (middle), where it is subdivided through arrangement with the new connectivity to generate intersection endpoints. This yields the tracked curve on the output mesh (right) with preserved topology.

On the other hand, we first then map p' to the parametric domain using barycentric interpolation

$$\mathbf{u}' = \sum_{j=0}^d b'_j \mathbf{u}_{v_j}, \quad (10)$$

where $\mathbf{u}_{v_j} \in U_i$ are the parametric coordinates of the vertices of t' .

We then locate the simplex $t \in \mathcal{P}_i^{\text{before}}$ containing \mathbf{u}' and compute its barycentric coordinates \mathbf{b} in t to obtain the result $p = (t, \mathbf{b})$.

The correctness follows from the fact that both $\mathcal{P}_i^{\text{before}}$ and $\mathcal{P}_i^{\text{after}}$ share the same geometric boundary and are embedded into the same parametric domain U_i , ensuring that any point $\mathbf{u}' \in U_i$ has a well-defined interpretation in both mesh states.

3.2.2 Curve Tracking. Curve Representation. The task of tracking piecewise-linear curves on \mathcal{M}' is not as trivial as simply projecting the endpoints of those curves to \mathcal{M} because a single linear segment might not lie on \mathcal{M} . In general, when the linear segments lie on more than one curve their embedding in 3D ceases to unambiguously lie on a mesh. As such, the inputs and outputs of our curve tracking procedure are piecewise linear curves are comprised of linear segments that each lie on a single simplex (triangle or tetrahedron), though multiple segments may exist in a single simplex. A curve C on a simplicial mesh is therefore represented as a sequence of segments:

$$C = \{\text{seg}_1, \text{seg}_2, \dots, \text{seg}_k\}, \quad (11)$$

where each segment seg_i is defined within a single simplex:

$$\text{seg}_i = (t_i, \mathbf{b}_i^{(1)}, \mathbf{b}_i^{(2)}), \quad (12)$$

with t_i being the simplex and $\mathbf{b}_i^{(1)}, \mathbf{b}_i^{(2)}$ the barycentric coordinates of the two endpoints. We require that consecutive segments are connected: the second endpoint of seg_i coincides with the first endpoint of seg_{i+1} , i.e., $(t_i, \mathbf{b}_i^{(2)}) \equiv (t_{i+1}, \mathbf{b}_{i+1}^{(1)})$ as points on the mesh. We use \equiv because when segments end on simplex boundaries there are multiple triangles (respectively, tetrahedra) for which to construct barycentric coordinates from and we only care that the segment endpoints hold equivalent barycentric coordinates.

Backward Tracking Problem. Given a curve $C' = \{\text{seg}'_1, \dots, \text{seg}'_m\}$ on \mathcal{M}_i and a local atlas $(U_i, \mathcal{P}_i^{\text{before}}, \mathcal{P}_i^{\text{after}})$, we seek to compute the pre-image curve $C = \{\text{seg}_1, \dots, \text{seg}_n\}$ on \mathcal{M}_{i-1} . Since the connectivity changes within the local patch, a segment in C' that lies entirely within a single simplex in $\mathcal{P}_i^{\text{after}}$ may intersect multiple simplices in $\mathcal{P}_i^{\text{before}}$ due to the different mesh topology. As such, a single segment

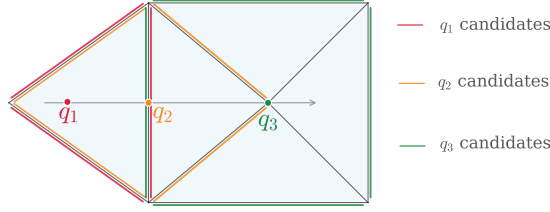


Fig. 8. Candidate facet selection during curve tracking: Given three query points q_1, q_2, q_3 along a ray, we select candidate edges (highlighted in color) based on each point’s location. Point q_1 lies in the interior of a triangle, so all three edges are candidates. Point q_2 lies on an edge, so candidates come from the link of that edge (opposite edges from incident triangles). Point q_3 lies at a vertex, so candidates are edges opposite to that vertex in all incident triangles. The algorithm selects the intersection with the smallest positive parameter t to advance to the next point.

in C' may result in multiple segments in C to guarantee that each segment of C lies in a single simplex in \mathcal{M} .

Segment Arrangement Algorithm. We perform our segment arrangement in the joint parametric space, so for a given segment $(t', \mathbf{b}'^{(1)}, \mathbf{b}'^{(2)})$ with $t' \in \mathcal{P}_i^{\text{after}}$, we map its endpoints to the parametric domain via (10), yielding parametric positions $\mathbf{u}^{(1)}$ and $\mathbf{u}^{(2)}$.

Our goal is to compute the arrangement of the segment $[\mathbf{u}^{(1)}, \mathbf{u}^{(2)}]$ with respect to $\mathcal{P}_i^{\text{before}}$ in the joint parametric space U_i . To do this employ a ray-marching: starting from $\mathbf{u}^{(1)}$, we trace along direction $\mathbf{k} = \mathbf{u}^{(2)} - \mathbf{u}^{(1)}$ until reaching $\mathbf{u}^{(2)}$, computing intersections with simplex boundaries (edges for 2D, faces for 3D) in $\mathcal{P}_i^{\text{before}}$ at each step. These intersection points will all lie on simplex boundaries, yielding sub-segments $\{\widetilde{\text{seg}}_1, \dots, \widetilde{\text{seg}}_\ell\}$ where each lies entirely within a single simplex of $\mathcal{P}_i^{\text{before}}$ (Figure 7).

Intersection Candidate Selection. At each step, given the current position \mathbf{V} in the parametric domain and direction \mathbf{k} , we determine candidate facets (edges for 2D, faces for 3D) based on the location of \mathbf{V} (Figure 8).

If \mathbf{V} lies strictly inside a simplex t , the candidates are all $(d-1)$ -dimensional facets of t : three edges for triangles, four faces for tetrahedra.

If \mathbf{V} lies on a lower-dimensional sub-simplex σ (a vertex, an edge for 2D/3D, or a face for 3D), we collect candidates from the link [Munkres 2018] of σ , i.e all $(d-1)$ -dimensional facets from simplices incident to σ excluding those facets that contain σ itself.

- **In 2D:** if σ is an edge (i, j) , then $\text{link}((i, j))$ includes the opposite edges from all triangles sharing (i, j) . If σ is a vertex v , then $\text{link}(v)$ includes all edges opposite to v in triangles containing v .
- **In 3D:** if σ is a face, then $\text{link}(\sigma)$ includes the opposite faces from tetrahedra sharing that face. If σ is an edge, then $\text{link}(\sigma)$ includes all faces from incident tetrahedra that do not contain the edge. If σ is a vertex v , then $\text{link}(v)$ includes all faces opposite to v in tetrahedra containing v .

Ray-Facet Intersection. For each candidate facet f , we compute the ray-facet intersection (ray-edge for 2D, ray-triangle for 3D) and select the one with smallest positive parameter $t > 0$ as the next intersection point. The detailed formulation is provided in

Appendix A.3. This process repeats until reaching $\mathbf{u}^{(2)}$, producing the sub-segments $\{\widetilde{\text{seg}}_1, \dots, \widetilde{\text{seg}}_\ell\}$ in $\mathcal{P}_i^{\text{before}}$.

3.2.3 Topology-Preserving Multi-Curve Tracking. In applications such as tracking UV seams or material boundaries on triangle meshes, we will need to track multiple curves or loops simultaneously. In such scenarios, the primary requirement is preserving the topological relationships among curves. Specifically, this means maintaining their intersection and overlap patterns in the correct order. Although our maps are bijective, running our procedure using floating point arithmetic occasionally changes the topological relationships between curves. On the other hand, exact rational arithmetic becomes computationally prohibitive. To balance these two extremes we take the approach of defining invariants that can help us determine whether a floating point computation introduced topological changes, and if a topological change does occur we re-run our tracking algorithm using exact rational predicates.

Intersection and Overlap Events. Consider a set of curves $C = \{C_1, \dots, C_\ell\}$ to be tracked. As we traverse a curve C_i from start to end, it encounters a sequence of events where it interacts with other curves (including itself for self-intersections). We classify these events into two types:

- **Intersection:** Two segments cross at a single point (either at shared endpoints or at a transversal intersection within a common simplex).
- **Overlap:** Two segments coincide along a positive-length interval (not just a single point).

For each curve C_i , we record the ordered sequence of events:

$$\mathcal{E}(C_i) = \langle e_1, e_2, \dots, e_m \rangle, \quad (13)$$

where each event e_k specifies:

- The type (intersection or overlap),
- The interacting curve index j (where j may equal i for self-interactions),
- The parametric location(s) along C_i where the event occurs.

Topology Preservation Requirement. Our goal is to ensure that for each curve $C_i \in C$ and its tracked result C'_i , the event sequence is preserved:

$$\mathcal{E}(C_i) \cong \mathcal{E}(C'_i), \quad (14)$$

where \cong denotes combinatorial equivalence: the sequences have the same length, and corresponding events have the same type and involve the same curve pairs.

Since intersections and overlaps are defined intrinsically within each simplex, we verify topology preservation locally for each operation. After tracking all curves through the local atlas $(U_i, \mathcal{P}_i^{\text{before}}, \mathcal{P}_i^{\text{after}})$, we compute the event sequences in $\mathcal{P}_i^{\text{before}}$ and verify that they match the original sequences in $\mathcal{P}_i^{\text{after}}$.

Implementation Strategy. We track all curves within a local patch simultaneously and extract their event sequences by:

- (1) For each pair of curves (C_i, C_j) (including $i = j$), enumerate all segment pairs and classify their interactions.
- (2) Sort events along each curve according to their parametric positions.
- (3) Compare the resulting event sequences before and after tracking.

If the event sequences do not match, typically due to numerical errors in double-precision arithmetic, we re-run tracking using exact rational arithmetic to ensure correctness.

Curve Simplification via Edge Collapse. To improve efficiency when tracking many curves over long remeshing sequences, we simplify curves by collapsing short segments. Given a segment $\text{seg} = (t, \mathbf{b}^{(1)}, \mathbf{b}^{(2)})$ with parametric length below a threshold ϵ , we consider collapsing it by merging its endpoints.

Crucially, edge collapse must preserve the event sequences $\mathcal{E}(C_i)$ for all curves. Before collapsing a segment in curve C_i , we verify that the local event sequence near the segment (including events involving C_i and other curves) remains unchanged after collapse and that no new intersections or overlaps are created, and no existing ones are destroyed.

This verification can be performed by computing event sequences in a local neighborhood before and after each potential collapse. By iteratively simplifying curves while preserving their event sequences, we significantly reduce computational cost without compromising topological correctness.

3.2.4 Surface Tracking on Tetrahedral Meshes. For tetrahedral meshes, we extend the tracking framework to handle surfaces, which are essential for applications such as tracking material interfaces or segmentation boundaries in volumetric simulations.

Surface Representation. A surface S on a tetrahedral mesh is represented as a triangle mesh embedded in the volume, where each vertex is a point on the tetrahedral mesh:

$$p = (t, \mathbf{b}), \quad (15)$$

with t being a simplex(tetrahedron) ID and $\mathbf{b} = (b_0, b_1, b_2, b_3)$ the barycentric coordinates. The surface consists of triangular faces:

$$S = \{f_1, f_2, \dots, f_k\}, \quad (16)$$

where each face $f_i = (p_i^{(1)}, p_i^{(2)}, p_i^{(3)})$ is defined by three vertices. We require that all three vertices of each face lie within the same tetrahedron, including its boundary. That is, if $p_i^{(j)} = (t_i^{(j)}, \mathbf{b}_i^{(j)})$ for $j \in \{1, 2, 3\}$, then either $t_i^{(1)} = t_i^{(2)} = t_i^{(3)}$, or they share a common face, edge, or vertex of the tetrahedral mesh.

Surface Arrangement Algorithm. Given a surface S' on \mathcal{M}_i and a local atlas $(U_i, \mathcal{P}_i^{\text{before}}, \mathcal{P}_i^{\text{after}})$, we track the portion of S' that intersects the local patch $\mathcal{P}_i^{\text{after}}$.

For each face $f \in S'$ with $f \subset \mathcal{P}_i^{\text{after}}$, we:

- (1) Map the three vertices of f to the parametric domain U_i , obtaining a triangle \tilde{f} in the parametric domain.
- (2) Extract the boundary surface of $\mathcal{P}_i^{\text{before}}$ restricted to the region covered by \tilde{f} .
- (3) Compute the arrangement of \tilde{f} with the boundary triangles of $\mathcal{P}_i^{\text{before}}$ using the `autorefine_triangle_soup` function from CGAL [Coeurjolly et al. 2025], which subdivides overlapping triangles into non-overlapping pieces and retriangulates the result.
- (4) Convert the resulting triangles back to barycentric coordinates with respect to tetrahedra in $\mathcal{P}_i^{\text{before}}$.

The CGAL arrangement procedure [The CGAL Project 2025] guarantees that the output is a valid triangulation where each triangle lies entirely within a single tetrahedron or on its boundary. To ensure robustness, this computation can be performed using exact rational arithmetic.

Topology Preservation for Multiple Surfaces. When tracking multiple surfaces $\mathcal{S} = \{S_1, \dots, S_m\}$ simultaneously, we preserve their topological relationships through an intersection structure between intersecting surfaces.

Just like with curve tracking, we will guarantee topology by developing an invariant. For surfaces, the relevant topological invariant is the number and connectivity of intersection curves. If surfaces S_i and S_j intersect, their intersection forms a set of curves (possibly multiple disjoint components). We define the *intersection graph* $\mathcal{G}(\mathcal{S})$ where:

- Nodes represent connected components of pairwise surface intersections.
- Edges connect components that share endpoints or form junctions.

Our goal is to ensure that, for the tracked surfaces S' , the intersection graph remains combinatorially equivalent: $\mathcal{G}(\mathcal{S}) \cong \mathcal{G}(S')$.

Surface Simplification via Edge Collapse. Similar to curve tracking, we simplify surface representations by collapsing short edges to improve efficiency. Given an edge $e = (p^{(1)}, p^{(2)})$ in a surface, we collapse it if its length is below a threshold ϵ , if the collapse keeps all incident triangles remain within a single tetrahedron or its boundary, and if the intersection graph $\mathcal{G}(\mathcal{S})$ is preserved.

To verify topology preservation, we compute the number of connected components in the intersection curves before and after collapse. If the component count changes, we reject the collapse. By iteratively applying valid collapses, we maintain a simplified surface representation throughout the tracking process without compromising topological correctness.

4 Results

4.1 Texture Transfer

A practical application of our point tracking framework is texture transfer across remeshed models (Figures 9 and 10). Given an input mesh with an existing UV parameterization and texture, our goal is to generate equivalent textures for remeshed versions of the model that may use entirely different parameterizations.

The key insight is that our bijective mapping decouples remeshing from UV maintenance. Traditional approaches must carefully preserve UV coordinates throughout remeshing operations, which becomes increasingly difficult when the mesh contains complex UV seams or multiple charts [Sander et al. 2001]. In contrast, our method allows the remeshed model to be reparameterized independently of any choice in standard parameterization algorithm. The texture is then transferred by composing the new parameterization with our tracked bijective correspondence: we evaluate each texel in the new texture domain by first mapping to the remeshed surface, tracking it backward to the original mesh, and finally sample the original texture at the corresponding UV coordinates.

Figures 9 and 10 demonstrate texture transfer through both mesh decimation and refinement operations. The center images show the

original models with their input UV parameterizations and textures. The top row displays the remeshed results after decimation (left) and refinement (right), both rendered with successfully transferred textures. The bottom row shows the UV layouts and corresponding texture maps generated for each remeshed model. Despite significant changes in mesh resolution and connectivity our bijective framework ensures accurate texture correspondence without introducing artifacts such as seam tearing or texture deviation.

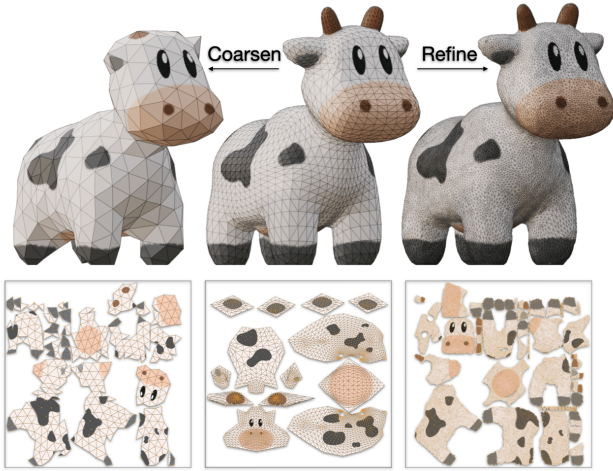


Fig. 9. Texture transfer through mesh decimation and refinement. **Center:** the input spotted animal model [Crane et al. 2013] with its original UV parameterization and texture. **Top row:** remeshed results after decimation (left) and refinement (right), rendered with the transferred texture. **Bottom row:** the UV layouts and generated textures corresponding to fresh parameterizations of each remeshed model. Our bijective mapping enables texture transfer by composing the new parameterization with the tracked correspondence, eliminating the need to maintain UV coordinates during remeshing operations.

4.2 Curve Tracking on Triangle Meshes.

We demonstrate our curve tracking algorithm on triangle meshes undergoing remeshing operations (Figure 11). Given an input mesh $\mathcal{M}_{\text{input}}$, we generate a collection of curves by intersecting the surface with axis-aligned planes parallel to the xy , yz , and xz coordinate planes. These curves form a complex network with several intersection points where curves from different plane families cross each other.

We then perform forward tracking through the remeshing sequence to obtain the corresponding curves on $\mathcal{M}_{\text{output}}$. As shown in Figure 11, the tracked curves faithfully preserve their intersection topology: the combinatorial pattern of curve crossings remains identical between input and output, with no spurious intersections introduced and no existing intersections lost. This topological guarantee is achieved through our topology-preserving multi-curve tracking algorithm (Section 3.2.3), which maintains ordered sequences of intersection events throughout the tracking process. Critically, during the segment arrangement phase, we employ exact arithmetic with coordinates represented as rational numbers to evaluate geometric

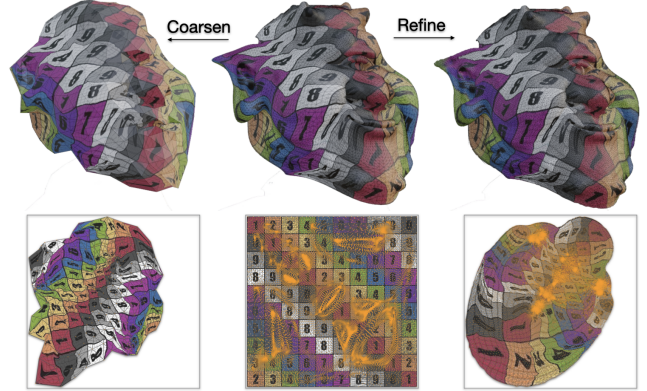


Fig. 10. Texture transfer on the Ogre model with checkerboard pattern. The regular grid structure of the checkerboard provides a visual metric for evaluating mapping quality and distortion. Despite extensive geometric and connectivity changes from decimation (top left) and refinement (top right), the checkerboard pattern remains smooth and continuous, demonstrating effective distortion control through our bijective framework.

predicates, ensuring numerical robustness and preventing topological inconsistencies that could arise from floating-point rounding errors.

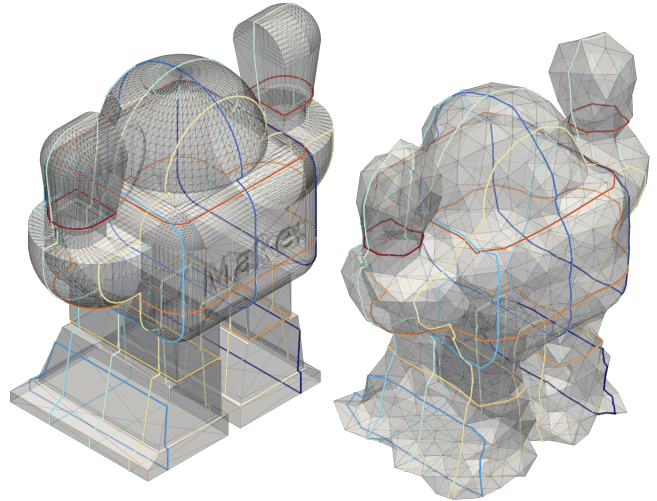


Fig. 11. Curve tracking on a triangle mesh. **Left:** curves on the input mesh $\mathcal{M}_{\text{input}}$, obtained as intersections of the surface with axis-aligned planes (parallel to the xy , yz , and xz planes), shown in distinct colors. **Right:** the forward-tracked curves on the output mesh $\mathcal{M}_{\text{output}}$ after isotropic remeshing. Our method preserves the intersection topology of the curves throughout the remeshing sequence—curves that intersect on the input mesh maintain their intersection relationships on the output mesh.

We evaluated our curve tracking algorithm on 5,139 manifold triangle meshes from the Thingi10K dataset [Zhou and Jacobson 2016]. For each model, we performed isotropic remeshing and tracked axis-aligned planar curves through the operation sequence. Of these

models, 4,998 (97.3%) completed successfully with topology preservation verified throughout. The remaining 141 models timed out after 12 hours, primarily due to extensive operation counts exceeding 700,000 per model. These timeouts represent computational resource limits rather than algorithmic failures—given sufficient computation time, they would yield topologically correct results identical to the successful cases. Furthermore, as we note in Section 5, the majority of this cost is due to computing each atlas as part of each topological operation. In reality this could be performed afterwards and in parallel.

Figure 12 showcases stress test examples where meshes undergo aggressive simplification with dramatic geometric changes. Despite surface features being substantially altered or eliminated, our method maintains topologically correct curve tracking—intersection patterns and connectivity remain intact. This demonstrates that our bijective framework preserves topological coherence even under severe geometric deformations: as long as the remeshing operations are topologically valid, our composed mappings produce correspondingly coherent results.

4.3 Surface Tracking on Tetrahedral Meshes

We demonstrate the application of our surface tracking framework to medical imaging data, specifically tracking organ segmentation boundaries through volumetric mesh simplification (Figure 13).

Our input data is derived from the CTA Abdomen (Panoramix) sample dataset provided in 3D Slicer. We obtain organ segmentations using TotalSegmentator [Wasserthal et al. 2023], a deep learning-based tool for automatic whole-body CT segmentation. We extract the surface triangulation of six major organs (heart, liver, gallbladder, stomach, and kidneys) as separate surfaces to be tracked, with each surface embedded in the volumetric mesh via barycentric coordinates.

We perform mesh simplification on the background body mesh while tracking the organ surfaces through each local atlas. As shown in Figure 13, the tracked organ surfaces maintain their geometric shapes and relative positions after simplification. The topological relationships among organs are preserved: surfaces that were previously disjoint remain non-intersecting throughout the remeshing sequence.

To evaluate surface tracking on a broader range of geometric models, we perform large-scale testing on tetrahedral meshes generated from the Thingi10K dataset [Zhou and Jacobson 2016] using TetWild [Hu et al. 2018] (Figure 1). For each input model, we first perform mesh simplification to obtain a coarsened output mesh $\mathcal{M}_{\text{output}}$. We then sample axis-aligned planar surfaces on this simplified mesh by intersecting it with planes parallel to the xy , xz , and yz coordinate planes.

We perform backward tracking to map these surfaces from $\mathcal{M}_{\text{output}}$ to the original high-resolution mesh $\mathcal{M}_{\text{input}}$. Critically, the intersection topology is preserved throughout the tracking process: the intersection graph $\mathcal{G}(S)$ representing how surfaces intersect remains combinatorially equivalent. As shown in Figure 1, surfaces that intersect on the simplified output mesh maintain their intersection relationships when back-tracked to the input mesh, with intersection curves faithfully reconstructed.

5 Conclusions

We have presented BijectiveRemesh, a robust framework for maintaining bijective mappings throughout complex remeshing sequences on both 2D triangle meshes and 3D tetrahedral meshes. Our approach guarantees global bijectivity through local atlas construction using two key innovations: shared scaffold structures for 2D operations and convex polyhedra embeddings for 3D boundary operations. These bijective mappings enable exact tracking of geometric entities—points, curves, and surfaces—with rigorous preservation of topological relationships, eliminating the artifacts common in projection-based transfer methods.

Limitations and Future Work. Constructing the bijective local atlases adds approximately 110× overhead per operation compared to performing remeshing operations alone. This overhead reflects the fact that our prototype augments each local patch with the auxiliary triangulation and performs iterative energy minimization with inversion-preventing line searches. We believe a substantial proportion of this overhead can be reduced through parallelization. Our current prototype implementation processes operations serially—constructing each local atlas sequentially as operations are applied. In practice, the atlas construction for different operations is independent: we can first record the local patch information for all operations during remeshing, then construct their corresponding local atlases in parallel. Since each operation’s atlas construction is self-contained, this parallel formulation would reduce total execution time.

We currently also depend on exact rational arithmetic for geometric predicates in our current tracking implementation for the sake of robustness. While we employ various optimizations including rounding to double and curve simplification, the computational overhead of performing long sequences of rational arithmetic remains substantial, making the tracking process can become prohibitively slow.

Our framework is designed for incremental, local-modification remeshing pipelines (edge splits, collapses, flips, and vertex smoothing). Global remeshing strategies—such as voxelization-based remeshing, Delaunay re-triangulation, or neural mesh extraction—do not decompose into sequences of local operations and are therefore outside the current scope. Extending bijective mapping maintenance to such non-incremental methods would require fundamentally different techniques and remains an open problem.

An important direction for future work is developing floating-point tracking algorithms that maintain topological guarantees without exact arithmetic. This would require novel geometric predicates and consistency checks that can tolerate numerical errors while still preventing topological corruption in the tracked curves and surfaces.

References

- Marc Alexa. 2023. Tutte Embeddings of Tetrahedral Meshes. *Discrete & Computational Geometry* 73 (2023), 197–207.
- Mario Botsch, Leif Kobbelt, Mark Pauly, Pierre Alliez, and Bruno Lévy. 2010. *Polygon mesh processing*. CRC press.
- Marcel Campen, Cláudio T. Silva, and Denis Zorin. 2016. Bijective maps from simplicial foliations. *ACM Transactions on Graphics* 35, 4 (2016), 74:1–74:15.
- David Coeurjolly, Jaques-Olivier Lachaud, Konstantinos Katrioplas, Sébastien Lorient, Ivan Paden, Mael Rouxel-Labbé, Hossam Saeed, Jane Tournois, Sébastien Valette, and Ilker O. Yaz. 2025. Polygon Mesh Processing. In *CGAL User and Reference*

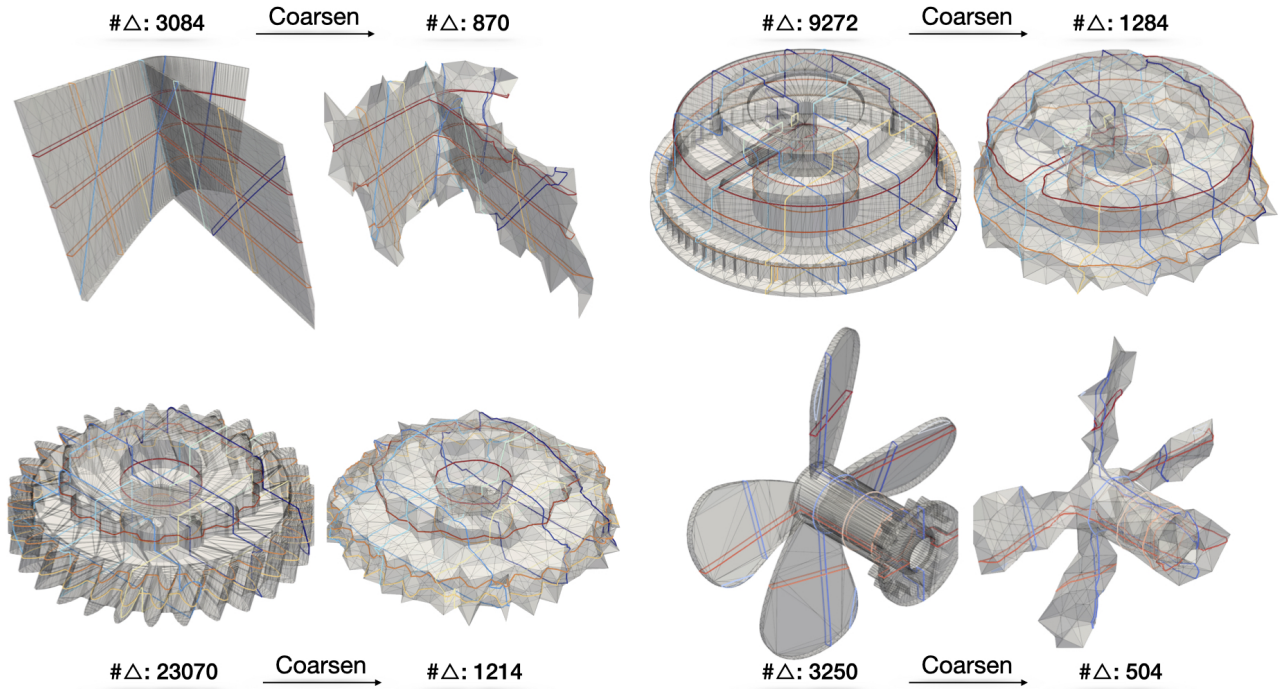


Fig. 12. Stress test for curve tracking under extreme remeshing. Each pair shows input mesh (left) and aggressively simplified output (right) with tracked curves in color. Despite dramatic geometric changes, our method preserves topological correctness—curve intersections and connectivity remain intact throughout. Thingi10K models: #636811 (top-left), #1036656 (top-right), #1312974 (bottom-left), #1505135 (bottom-right).

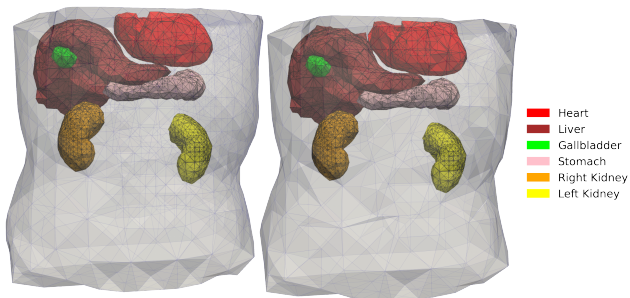


Fig. 13. Surface tracking on a tetrahedral body mesh from CT scan data. We track multiple organ segmentation surfaces (heart, liver, gallbladder, stomach, and kidneys) through volumetric mesh simplification. **Left:** organ surfaces on the input tetrahedral mesh M_{input} . **Right:** the tracked surfaces on the simplified output mesh M_{output} . Our bijective framework maintains the topological relationships among organs throughout the remeshing process.

Manual (6.1 ed.). CGAL Editorial Board. <https://doc.cgal.org/6.1/Manual/packages.html#PkgPolygonMeshProcessing>
 Keenan Crane, Ulrich Pinkall, and Peter Schröder. 2013. Robust fairing via conformal curvature flow. *ACM Transactions on Graphics (TOG)* 32, 4 (2013), 1–10.
 Xingyi Du, Noam Aigerman, Qingnan Zhou, Shahar Z Kovalsky, Yajie Yan, Danny M Kaufman, and Tao Ju. 2020. Lifting simplices to find injectivity. *ACM Trans. Graph.* 39, 4 (2020), 120.

Danielle Ezuz, Justin Solomon, and Mirela Ben-Chen. 2019. Reversible Harmonic Maps between Discrete Surfaces. *ACM Transactions on Graphics* 38, 2 (2019).
 Michael S. Floater. 2003. One-to-one piecewise linear mappings over triangulations. *Math. Comp.* 72, 242 (2003), 685–696.
 Michael S. Floater and Valérie Pham-Trong. 2006. Convex combination maps over triangulations, tilings, and tetrahedral meshes. *Advances in Computational Mathematics* 25, 4 (2006), 347–356.
 Xiao-Ming Fu, Yang Liu, and Baining Guo. 2015. Computing locally injective mappings by advanced MIPS. *ACM Transactions on Graphics (TOG)* 34, 4 (2015), 1–12.
 Yixin Hu, Qingnan Zhou, Xifeng Gao, Alec Jacobson, Denis Zorin, and Daniele Panozzo. 2018. Tetrahedral Meshing in the Wild. *ACM Trans. Graph.* 37, 4, Article 60 (July 2018), 14 pages. doi:10.1145/3197517.3201353
 Zhongshi Jiang, Scott Schaefer, and Daniele Panozzo. 2017. Simplicial complex augmentation framework for bijective maps. *ACM Transactions on Graphics* 36, 6 (2017), 186:1–186:9.
 Zhongshi Jiang, Teseo Schneider, Denis Zorin, and Daniele Panozzo. 2020. Bijective Projection in a Shell. *ACM Transactions on Graphics* 39, 6 (2020).
 Zhongshi Jiang, Ziyi Zhang, Yixin Hu, Teseo Schneider, Denis Zorin, and Daniele Panozzo. 2021. Bijective and Coarse High-Order Tetrahedral Meshes. *ACM Transactions on Graphics* 40, 4 (2021).
 Leif Kobbelt, Swen Campagna, Jens Vorsatz, and Hans-Peter Seidel. 1998. Interactive multi-resolution modeling of arbitrary meshes. *SIGGRAPH (1998)*, 105–114.
 Vladislav Kraevoy and Alla Sheffer. 2004. Cross-parameterization and compatible remeshing of 3D models. *ACM Transactions on Graphics (TOG)* 23, 3 (2004), 861–869.
 Yaron Lipman. 2014. Bijective Mappings of Meshes with Boundary and the Degree in Mesh Processing. *SIAM Journal on Imaging Sciences* 7, 2 (2014), 1263–1283.
 Hsueh-Ti Derek Liu, Jiayi Eris Zhang, Mirela Ben-Chen, and Alec Jacobson. 2021. Surface multigrid via intrinsic prolongation. *ACM Trans. Graph.* 40, 4, Article 80 (jul 2021), 13 pages. doi:10.1145/3450626.3459768
 Filippo Maggioli, Daniele Baieri, Emanuele Rodolà, and Simone Melzi. 2024. Rematching: Low-resolution representations for scalable shape correspondence. 183–200 pages.
 James R. Munkres. 2018. *Elements of Algebraic Topology*. CRC Press. doi:10.1201/9780429493911

- Valentin Z. Nigolian, Marcel Campen, and David Bommes. 2023. Expansion Cones: A Progressive Volumetric Mapping Framework. *ACM Transactions on Graphics* 42, 4 (2023).
- Valentin Z. Nigolian, Marcel Campen, and David Bommes. 2024. A Progressive Embedding Approach to Bijective Tetrahedral Maps driven by Cluster Mesh Topology. *ACM Transactions on Graphics* 43, 6 (2024).
- Michael Rabinovich, Roi Poranne, Daniele Panozzo, and Olga Sorkine-Hornung. 2017. Scalable Locally Injective Mappings. *ACM Transactions on Graphics* 36, 2 (2017).
- Ares Ribó Mor, Günter Rote, and André Schulz. 2011. Small grid embeddings of 3-polytopes. *Discrete & Computational Geometry* 45, 1 (2011), 65–87.
- Pedro V Sander, John Snyder, Steven J Gortler, and Hugues Hoppe. 2001. Texture mapping progressive meshes. In *Proceedings of the 28th annual conference on Computer graphics and interactive techniques*. 409–416.
- Patrick Schmidt, Dörte Pieper, and Leif Kobbelt. 2023. Surface Maps via Adaptive Triangulations. *Computer Graphics Forum* 42, 2 (2023).
- Jason Smith and Scott Schaefer. 2015. Bijective parameterization with free boundaries. *ACM Transactions on Graphics (TOG)* 34, 4 (2015), 1–9.
- Olga Sorkine and Marc Alexa. 2007. As-rigid-as-possible surface modeling. In *Symposium on Geometry Processing*, Vol. 4. 109–116.
- Ernst Steinitz. 1922. Polyeder und Raumteilungen. In *Encyklopädie der Mathematischen Wissenschaften*. Vol. 3.
- The CGAL Project. 2025. *CGAL User and Reference Manual* (6.1 ed.). CGAL Editorial Board. <https://doc.cgal.org/6.1/Manual/packages.html>
- William T. Tutte. 1963. How to Draw a Graph. *Proceedings of the London Mathematical Society* 13, 1 (1963), 743–767.
- Jakob Wasserthal, Hanns-Christian Breit, Manfred T Meyer, Maurice Pradella, Daniel Hinck, Alexander W Sauter, Tobias Heye, Daniel T Boll, Joshy Cyriac, Shan Yang, et al. 2023. TotalSegmentator: robust segmentation of 104 anatomic structures in CT images. *Radiology: Artificial Intelligence* 5, 5 (2023), e230024.
- Qingnan Zhou and Alec Jacobson. 2016. Thingi10K: A Dataset of 10,000 3D-Printing Models. *arXiv preprint arXiv:1605.04797* (2016).

A Appendix

A.1 Constructive Algorithms for Convex Polyhedra Embedding

The following two algorithms describe the constructive procedure for embedding a planar graph as a convex polyhedron, as referenced in Section 3.1.3. Algorithm 1 computes a crossing-free planar embedding via Tutte’s barycentric method, and Algorithm 2 lifts it into a 3D convex polyhedron via the Maxwell-Cremona correspondence.

Algorithm 1 Tutte Barycentric Embedding

Input: Planar graph given by face list $F = \{f_1, f_2, \dots\}$ and outer triangle $f_0 = (v_1, v_2, v_3)$

Output: 2D embedding $p : V \rightarrow \mathbb{R}^2$

Construct weighted Laplacian

- 1: **for** each undirected edge (i, j) **do**
- 2: $\omega_{ij} \leftarrow \begin{cases} 1, & \text{if } (i, j) \text{ is an interior edge,} \\ 0, & \text{if } i, j \in f_0 \end{cases}$
- 3: **end for**
- 4: Assemble the $n \times n$ weighted Laplacian: $L_{ii} = \sum_j \omega_{ij}$, $L_{ij} = -\omega_{ij}$ for $i \neq j$

Partition variables

- 5: Let B be the three boundary vertex indices in f_0 , and I be the interior vertices
- 6: Partition: $L = \begin{pmatrix} L_{BB} & L_{BI} \\ L_{IB} & L_{II} \end{pmatrix}$

Fix boundary vertices

- 7: $p_{v_1} \leftarrow (0, 0)$, $p_{v_2} \leftarrow (1, 0)$, $p_{v_3} \leftarrow (0, 1)$
- 8: $x_B \leftarrow (0, 1, 0)^\top$, $y_B \leftarrow (0, 0, 1)^\top$

Solve for interior vertices

- 9: Solve $L_{II}x_I = -L_{IB}x_B$ and $L_{II}y_I = -L_{IB}y_B$
- 10: **return** Crossing-free planar embedding $p : V \rightarrow \mathbb{R}^2$

Algorithm 2 Maxwell-Cremona Lifting to Convex Polyhedron

Input: Planar embedding $p : V \rightarrow \mathbb{R}^2$ from Algorithm 1

Output: Convex polyhedra embedding $\{(p_v, z_v) \mid v \in V\} \subset \mathbb{R}^3$

Assign equilibrium stress

- 1: **for** each interior edge (i, j) **do**
- 2: $\omega_{ij} \leftarrow 1$
- 3: **end for**

Define plane per face

For each face f_k , seek plane $H_k : z = \langle (x, y), a_k \rangle + d_k$

Maxwell-Cremona propagation

- 4: Choose one interior face f_1 as base: $a_1 \leftarrow (0, 0)$, $d_1 \leftarrow 0$
- 5: **for** each pair of adjacent faces f_r, f_ℓ sharing edge (i, j) **do**
- 6: where f_ℓ lies to the left of directed edge $i \rightarrow j$
- 7: $a_\ell \leftarrow \omega_{ij}(p_i - p_j)^\perp + a_r$ $\triangleright (x, y)^\perp = (-y, x)$
- 8: $d_\ell \leftarrow \omega_{ij}\langle p_i, (p_j)^\perp \rangle + d_r$
- 9: **end for**

Compute vertex heights

- 10: **for** each vertex $v \in V$ **do**
- 11: Pick any incident face f_k
- 12: $z_v \leftarrow \langle p_v, a_k \rangle + d_k$
- 13: **end for**
- 14: **return** Convex polyhedron $\{(p_v, z_v)\}$ whose projection onto xy -plane is the Tutte embedding

A.2 Non-overlapping via Convex Boundary Embedding

LEMMA A.1 (NON-OVERLAPPING VIA CONVEX BOUNDARY EMBEDDING). *Let $\mathcal{P}_{\text{before}}$ be the local patch of boundary tetrahedra incident to vertex i . The boundary of this patch consists of:*

- Face f_k : the one-ring of vertex i on $\partial\mathcal{M}_\ell$ (containing vertex i),

- Faces f_0, \dots, f_{k-1} : the k adjacent boundary triangles.

Suppose the vertices of $\{f_0, \dots, f_{k-1}, f_k\}$ (excluding i) are embedded to form a convex polyhedron C via Algorithms 1 and 2, where we select one triangle from $\{f_0, \dots, f_{k-1}\}$ as the outer boundary for the Tutte embedding.

Then for any position of vertex i on or inside face f_k , all tetrahedra in $\mathcal{P}_{\text{before}}$ are non-overlapping.

PROOF. A tetrahedral mesh is non-overlapping if and only if for every internal face, the two opposite vertices lie on opposite sides of that face.

Consider an arbitrary internal face $f = (i, v_a, v_b)$ shared by two tetrahedra $T_1 = (i, v_a, v_b, v_c)$ and $T_2 = (i, v_a, v_b, v_d)$. We must show that v_c and v_d lie on opposite sides of the plane Π containing f .

Key observation. The face $f = (i, v_a, v_b)$ contains the edge (v_a, v_b) , which is an edge of the convex polyhedron C . The vertices v_c and v_d are the two boundary vertices adjacent to this edge, forming boundary faces (v_a, v_b, v_c) and (v_a, v_b, v_d) of C .

Convexity guarantee. By the convexity of C , the dihedral angle at edge (v_a, v_b) is less than π . This means that for *any* plane Π containing edge (v_a, v_b) , the vertices v_c and v_d lie on opposite sides of Π .

In particular, since vertex i is positioned on or inside face f_k of the convex polyhedron C , and the plane Π through face (i, v_a, v_b) contains edge (v_a, v_b) , we have:

$$[(\mathbf{p}_c - \mathbf{p}_a) \cdot \mathbf{n}] \cdot [(\mathbf{p}_d - \mathbf{p}_a) \cdot \mathbf{n}] < 0,$$

where $\mathbf{n} = (\mathbf{p}_b - \mathbf{p}_a) \times (\mathbf{p}_i - \mathbf{p}_a)$ is the normal of Π .

Since this holds for every internal face, all tetrahedra in $\mathcal{P}_{\text{before}}$ are non-overlapping. \square

A.3 Ray-Facet Intersection Predicates

This section provides the ray-facet intersection predicates used in curve tracking (Section 3.2.2).

A.3.1 Ray-Edge Intersection (2D). Given a ray starting at $\mathbf{V} \in \mathbb{R}^2$ with direction \mathbf{k} , and an edge with endpoints $\mathbf{a}, \mathbf{b} \in \mathbb{R}^2$, we seek parameters t and u satisfying:

$$\mathbf{V} + t\mathbf{k} = \mathbf{a} + u(\mathbf{b} - \mathbf{a}). \quad (17)$$

Let $\mathbf{v}_1 = \mathbf{b} - \mathbf{a}$ and $\mathbf{v}_2 = \mathbf{a} - \mathbf{V}$. The determinant is:

$$\Delta = \mathbf{k}_x \mathbf{v}_1 y - \mathbf{k}_y \mathbf{v}_1 x. \quad (18)$$

If $\Delta \neq 0$:

$$t = \frac{\mathbf{v}_2 x \mathbf{v}_1 y - \mathbf{v}_2 y \mathbf{v}_1 x}{\Delta}, \quad u = \frac{\mathbf{k}_x \mathbf{v}_2 y - \mathbf{k}_y \mathbf{v}_2 x}{\Delta}. \quad (19)$$

An intersection exists if $t > 0$ and $u \in [0, 1]$.

A.3.2 Ray-Triangle Intersection (3D). Given a ray starting at $\mathbf{V} \in \mathbb{R}^3$ with direction \mathbf{k} , and a triangle with vertices $\mathbf{a}, \mathbf{b}, \mathbf{c} \in \mathbb{R}^3$, we compute the normal $\mathbf{n} = (\mathbf{b} - \mathbf{a}) \times (\mathbf{c} - \mathbf{a})$ and the ray-plane intersection:

$$t = \frac{\mathbf{n} \cdot (\mathbf{a} - \mathbf{V})}{\mathbf{n} \cdot \mathbf{k}}. \quad (20)$$

If $t > 0$, compute $\mathbf{p} = \mathbf{V} + t\mathbf{k}$ and its barycentric coordinates (w_0, w_1, w_2) with respect to $(\mathbf{a}, \mathbf{b}, \mathbf{c})$. The point lies inside the triangle if $w_i \geq 0$ for all i .

A.3.3 Implementation Notes. For robustness in topology-preserving curve tracking, these predicates should be evaluated using exact arithmetic. We represent all coordinates as rational numbers and perform all arithmetic operations exactly. While this incurs computational overhead, it guarantees that intersection tests are consistent and prevents numerical errors from violating topological invariants.

In practice, we first attempt intersection tests using double-precision floating-point arithmetic. If the result is near-degenerate (e.g., $\Delta \approx 0$ in 2D, or barycentric coordinates near boundary values), we fall back to exact rational arithmetic to ensure correctness.